



Full Length Article

Structure of tetrabrachial flames in non-premixed autoigniting dimethyl ether/air mixtures

Tai Jin^{a,b}, Xujiang Wang^a, Kai H. Luo^{a,*}, Kun Luo^b, Jianren Fan^b^a Department of Mechanical Engineering, University College London, London WC1E 7JE, United Kingdom^b State Key Laboratory of Clean Energy Utilization, Zhejiang University, Hangzhou 310027, PR China

ARTICLE INFO

Keywords:

Two-stage ignition
 Most reactive mixture
 Tetrabrachial flames
 Direct numerical simulation

ABSTRACT

Structures of tetrabrachial flames in two-stage autoigniting dimethyl ether (DME)/air mixture under diesel engine relevant conditions are investigated by direct numerical simulation. Three cases with different initial turbulent integral length scales are studied. Results show that the first stage of autoignition initiates in lean mixtures, and subsequently develops into a diffusion-supported cool flame propagating into rich mixtures; the second-stage autoignition features spatially distributed kernels in fuel-rich mixtures, followed by hybrid auto-ignition/tetrabrachial flames. The detailed chemical structures of the tetrabrachial flames are analyzed in terms of reactant concentrations and the reaction rate profiles. The cool flame branch is dominated by low temperature reactions, while the other branches are mainly involved in high temperature oxidation of the remaining fuel and intermediate species. The excess DME is consumed in the premixed flame branches and decomposed into more stable fuels including H₂, CH₄ and CO in the trailing diffusion flame, where H₂ and CO are mainly oxidized by intermediate species OH and O. The structures and reaction rates in the tetrabrachial flame exhibit significant asymmetry, which is more distinct in the mixture fraction-temperature phase space. Effects of turbulence on the timing and location of two-stage ignition are then studied. In this study, turbulence tends to advance ignition compared with laminar cases, while the first high-temperature ignition time is similar for the three cases with different initial turbulence integral length scales.

1. Introduction

Autoignition of fuel-air mixtures in a turbulent flow is a complex problem of great theoretical interest and also relevant to practical combustors, where ignition occurs after fuel injection in a high-pressure and high-temperature environment. A two-stage autoignition has been observed under conventional diesel engine conditions, involving pre-ignition reactions due to low-temperature chemistry (LTC), followed by the main ignition due to high-temperature chemistry (HTC) [1]. Conceptual models of diesel combustion, based on observations in optically accessible engines and chambers, have not yet been conclusively demonstrated [2,3]. Experimental observations still have limitations in simultaneous measurement of multiple parameters [4,5], especially in a combusting environment.

Tibrachial flames (also known as triple flames) present to facilitate the flame propagation during nonuniform ignition [6–8]. Domingo et al. [7] showed that tibrachial flame structures played a key role in the propagation of ignition along stoichiometric contours. Echehki et al. [8] detected the formation of tibrachial flames during the autoignition

of non-homogeneous mixtures of hydrogen in heated air. The tibrachial flame structure also provides a mechanism for partially premixed flame stabilization that may be present in lifted jet flames [9]. The stabilization, propagation, and instability of tibrachial flames in non-autoignitive conditions have been reviewed by Chung [10], and they further studied the tibrachial flames in autoignited conditions [11,12]. Practical hydrocarbon-based fuels generally have two-stage ignition process, and may exhibit the negative temperature coefficient (NTC) phenomena in the intermediate temperature regime [13]. The ignition characteristics of nonpremixed flames can be fundamentally affected by NTC effects, especially at elevated pressures. A transition from tibrachial to polybrachial flame structure has been found in partially premixed laminar DME/air jet flame, with various temperatures of the oxidizer [14]. The multibrachial flame structures are also observed by Deng et al. [15,16] in laminar DME/air coflow flames, and further investigations into the controlling chemistry are conducted based on Chemical Explosive Mode Analysis. Krisman et al. [17] have also reported that the edge flame in a two-stage igniting turbulent mixing layer has a hybrid structure consisting of a tetrabrachial flame.

* Corresponding author.

E-mail address: k.luo@ucl.ac.uk (K.H. Luo).

Nomenclature		turb	turbulent
Da	Damköhler number	ign	ignition
l	length scale (m)	st	stoichiometric
r	radius (m)	Od	zero dimensional
Re	Reynolds number	<i>Abbreviation</i>	
T	temperature (K)	CF	cool flame
t	time (s)	DME	dimethyl ether
u	velocity (m/s)	DF	diffusion flame
Y_k	mass fraction of species k	HTC	high-temperature chemistry
ξ	mixture fraction	HRR	heat release rate
χ	scalar dissipation rate	HIK	high-temperature ignition kernel
τ	ignition delay time (s)	LPF	lean premixed flame
δ	thickness of mixing layer (m)	LTC	low-temperature chemistry
<i>Subscript</i>		NTC	negative temperature coefficient
mr	most reactive	RPF	rich premixed flame

However, no detailed chemical structures have yet been analyzed.

Turbulence has been observed to affect the location and timing of autoignition in the mixing layer [18,19]. Experimental and numerical studies of single stage autoignition of non-premixed mixture in turbulent inhomogeneous flows at atmospheric conditions have revealed that autoignition kernels appear first at locations around most reactive mixture fraction ξ_{mr} [18,20–23], along with the lowest scalar dissipation rate χ . This has been confirmed in direct numerical simulation (DNS) studies with detailed chemical and transport models both in two- and three- dimensional turbulence [23,24]. Several DNS studies have been devoted to the investigation of ignition under diesel engine-relevant conditions with appropriate simplified assumptions. Yao et al. [25] investigated hydrogen/air autoignition in turbulent mixing layer at elevated pressures up to 30 atm and found that autoignition occurred at the most reactive mixture fraction isosurfaces. Borghesi et al. [26] conducted DNS of autoigniting n-heptane sparse spray at 24 bar with reduced chemistry. The doubly conditioned statistics revealed a two-stage autoignition. DNS of an igniting turbulent mixing layer of DME-air mixture was performed by Krisman et al. [17,27]. They found that ξ_{mr} calculated from the homogeneous reactor is not sufficient to predict the location of the second stage autoignition. This is also proved in a further 3D DNS of a temporally evolving planar jet of n-heptane at 40 atm with global chemistry by Krisman et al. [28].

Despite considerable progress made regarding two-stage autoignition, a complete clarification of the structure of the polybrachial flames is still lacking. Further detailed information on turbulence effects on two-stage autoignition would enhance our understanding of the underlying physical processes. The present DNS study considers ignition of a DME pocket in turbulent air at 40 atm within the NTC regime. The main objectives of the present work are to demonstrate the chemical structures of the tetrabrachial flames, as well as turbulent effects on ignition timing and locations in the DME/air mixture.

2. Configuration and numerical methods

The computational domain is sketched in Fig. 1, with a pocket of low temperature (400 K) pure DME exposed in high temperature air (composed of 21% O_2 and 79% N_2 , 900 K). The square two-dimensional domain has a size of 3.2 mm by 3.2 mm, and the radius of the fuel pocket is initialized as $r_0 = 0.8$ mm. The system has a pressure of 40 atm. The initial composition and temperature vary across a mixing layer with a specified hyperbolic tangent mixture fraction profile which is described as $\xi(r) = \left(1 + \tanh\left(\frac{r_0 - r}{\delta}\right)\right)/2$, where $\delta = 40$ μ m is the initial thickness of the mixing layer. Initial fuel and air profiles are set according to the mixing line while all other species are initially set to

zero.

Periodic boundary conditions are employed at all boundaries, to mimic the constant volume configuration. The Passot-Pouquet isotropic kinetic energy spectrum [17] is employed to generate the initial turbulent velocity field: $E(k) = \frac{32}{3} \sqrt{\frac{2}{\pi}} \frac{u'^2}{k_e} \left(\frac{k}{k_e}\right)^4 \exp\left[-2\left(\frac{k}{k_e}\right)^2\right]$, where k is the wave number, the subscript e is for the most energetic wave number, and u' is the root mean square (RMS) velocity. The generated velocity is then superimposed on the stationary mean flow field as the initial condition. The prescribed turbulence varies with the integral length scale l_t , while the initial RMS turbulent velocity fluctuations remain the same and are set equal to 0.5 m/s. The initial l_t equals 0.1, 0.2, and 0.4 mm for cases 1, 2 and 3, respectively. l_t is the only varied parameter for the three cases studied. The corresponding Damköhler numbers (Da) are 0.57, 1.14 and 2.28, where Da is defined as $Da = \tau_{turb} / \tau_{(\xi=\xi_{mr,0d})}$, τ_{turb} is the eddy time defined as $\tau_{turb} = l_t / u'$, $\tau_{(\xi=\xi_{mr,0d})}$ is the ignition delay time of the most reactive mixture measured in a homogeneous reactor, which is also used for non-dimensionalization of time t ($t^* = t / \tau_{(\xi=\xi_{mr,0d})}$).

The full compressible Navier-Stokes equations, species and energy conservation equations for a reacting gas mixture are solved with an in-house DNS code. A fourth-order explicit Runge-Kutta method for time integration and an eighth-order central differencing scheme for spatial discretization are used with a tenth-order filter for removing spurious

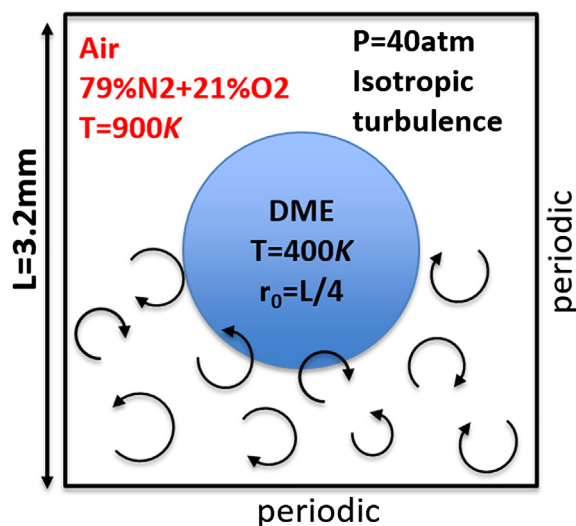


Fig. 1. Schematic of the computational configuration.

high frequency fluctuations in the solution. The mixture is assumed to be a perfect gas. CHEMKIN software libraries [29] are linked to the current code to evaluate reaction rates, as well as thermodynamic and transport properties for both the individual species and the averaged mixture. Detailed description of the DNS code is given in our previous publications [30,31]. A reduced chemical mechanism for DME oxidation consisting of 30 chemical species in 175 reaction steps is employed [32], which has been used in previous DNS studies of lifted laminar flames and turbulent mixing layers [14,17,27]. A very fine mesh is required to resolve the extremely thin flame under high pressure conditions. Based on previous studies by Krisman et al. [17,27], an equidistant mesh with a resolution of 1 μm in both directions is adopted here and the solution is advanced with a time step of 1 ns.

3. Results and discussion

3.1. Two-stage ignition process

The transient ignition process is illustrated by the instantaneous images of heat release rate (HRR) in Fig. 2. A general sequence of two-stage autoignition and transition from autoignition kernels to edge flame propagation can be found, which is consistent with previous DNS study of turbulent DME/air mixing layer by Krisman et al. [17,27]. The first stage autoignition due to low temperature chemistry reactions is initiated in the fuel lean mixture as in Fig. 2a, which is affected by the local scalar dissipation rate χ . Turbulent mixing induces a wide range of χ values. High χ values result in low heat release rate and even the absence of ignition, leading to a disconnected low temperature ignition front as shown in Fig. 2a. The LTC regions develop into a connected, wrinkled cool-flame that is supported by diffusion [27]. The cool-flame moves up the mixture fraction gradient into richer mixture, as shown in Fig. 2b–d. The first high-temperature ignition kernels (HIKs), as shown in Fig. 2b, formed in the rich mixture regions close to the black solid lines, which correspond to the most reactive mixture fraction ($\xi_{\text{mr},1\text{d}}$) related to the second stage ignition of the one-dimensional mixing layer and equal 0.205 as detailed in the [supplementary material](#) (where the DNS results of the 1d mixing layer are presented). More HIKs sequentially appear and are spatially randomly located. Most kernels have

qualitatively similar behaviors, forming in rich ξ . Thereafter, a thin circular flame front forms and burns through the mixing layer. As the flame penetrates the stoichiometric region, two edge flames are established and propagate in opposite directions along the ξ_{st} surface, as shown in Fig. 2c.

The edge flames have a main tribrachial (triple) flame composed of leading lean and rich premixed branches that merge at the triple point with a trailing non-premixed branch and the co-existing cool flame can be considered as a fourth branch of the edge flames. Some kernels merge with earlier-formed kernels, or are overtaken by propagating edge flames before they can reach ξ_{st} and establish additional edge flames, as shown in Fig. 2d–f. Besides, there is one extraordinary kernel formed at locally quite rich mixture (shown in Fig. 2d), which is caused by the collision of cool flame (CF) fronts. The lean premixed flames far away from the triple points gradually extinguish as shown in Fig. 2f, while the trailing diffusion flames survive for a longer period. It seems $\xi_{\text{mr},1\text{d}}$, other than $\xi_{\text{mr},0\text{d}}$ as discussed by Krisman et al. [17,27], can well predict the locations of the HIKs, which will be further analyzed through collected statistics of the location and timing of HIKs. It can also be found that the propagation and collision of triple flames play an essential role during the ignition process.

3.2. Tetrabrachial flame structures

A typical structure of the tetrabrachial flames is illustrated by the contours of temperature (T (K)), heat release rate (HRR (W/m^3)) and mixture fraction (ξ) in Fig. 3. High temperature products are located around the stoichiometric mixture. $Y_{\text{CH}_3\text{OCH}_2\text{O}_2}$ is closely associated with LTC HRR, and (which equals 20% of the maximum value of $Y_{\text{CH}_3\text{OCH}_2\text{O}_2}$) surface is a good marker of the cool flame. The profiles extracted at the cross-section A-A' downstream of the triple point are also shown in Fig. 4. Four peaks of HRR can be found, which correspond to the four branches of the edge flame, lean premixed flame (LPF), diffusion flame (DF), rich premixed flame (RPF) and cool flame (CF). In the present flame, HRR in the diffusion flame which corresponds to the high-temperature chemical reactions, is larger than the LPF and RPF. This differs from the previous findings in triple flames of CH_4 [33] and methanol [34], where the heat release rate in the diffusion flame is an order of

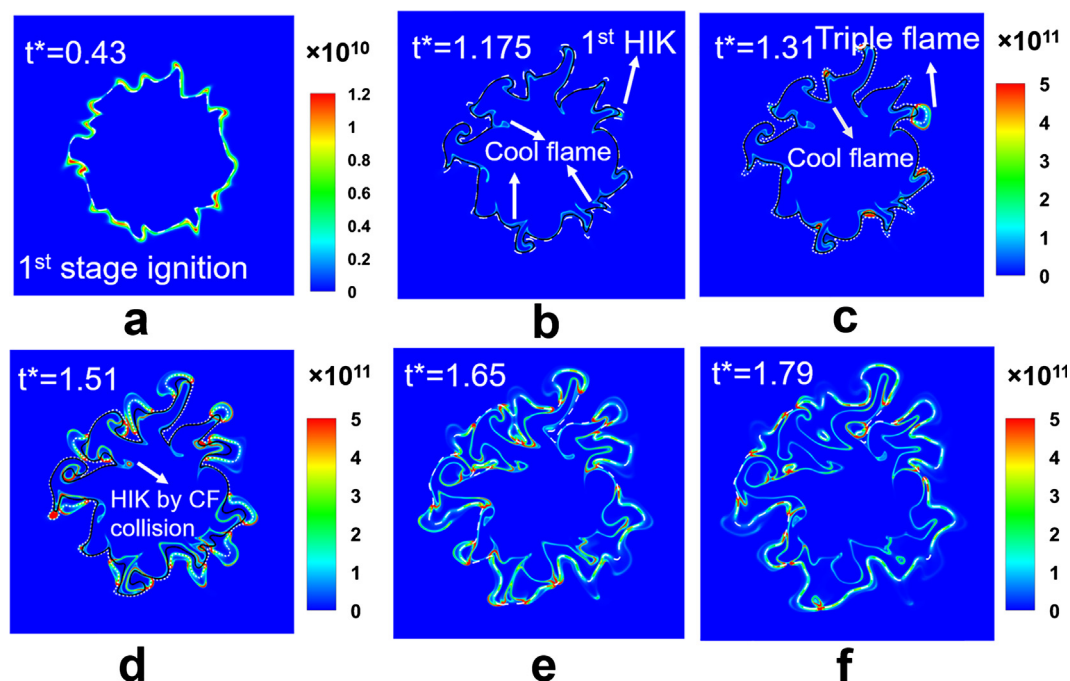


Fig. 2. Temporal evolution of heat release rate (HRR), W/m^3 . The non-dimensional time $t^* = t/\tau(\xi = \xi_{\text{mr},0\text{d}})$. The white dashed line is the ξ_{st} surface and the black solid line is the $\xi_{\text{mr},1\text{d}}$ surface, which is related to the second stage ignition of the 1D mixing layer.

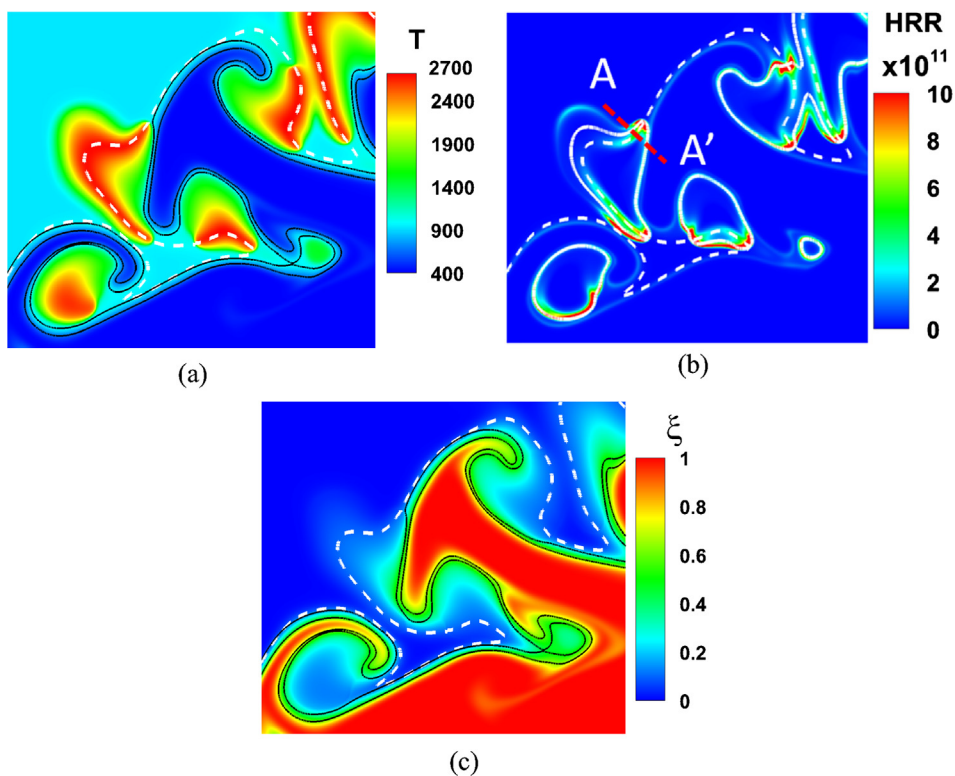


Fig. 3. Zoomed-in view of the tetrabrachial flame structure for case a at non-dimensional time $t^* = 1.54$. The white dashed line is the ξ_{st} surface, the black solid line is the $Y_{H_2O} = 0.08$ surface, the white solid line is the $Y_{CH_3OCH_2O_2} = 0.0784$ surface which is the marker of LTC.

magnitude smaller than in the premixed branches.

A detailed description of the chemical structure of the tetrabrachial flame is given in terms of reactant, radicals and their reaction rate profiles. The two-stage ignition process of DME is controlled by different chemical reactions. The first stage is controlled by competing, low temperature chemical pathways, and the second stage involves

rapid, thermal dissociation and oxidation of the remaining fuel and intermediate species produced from the first stage of ignition. As for the tetrabrachial flame, the cool flame branch is dominated by the low temperature reactions, while for the other three branches are mainly involved with the high temperature oxidation. Fig. 5 shows the isocontours of the reactants and products mass fractions, as well as

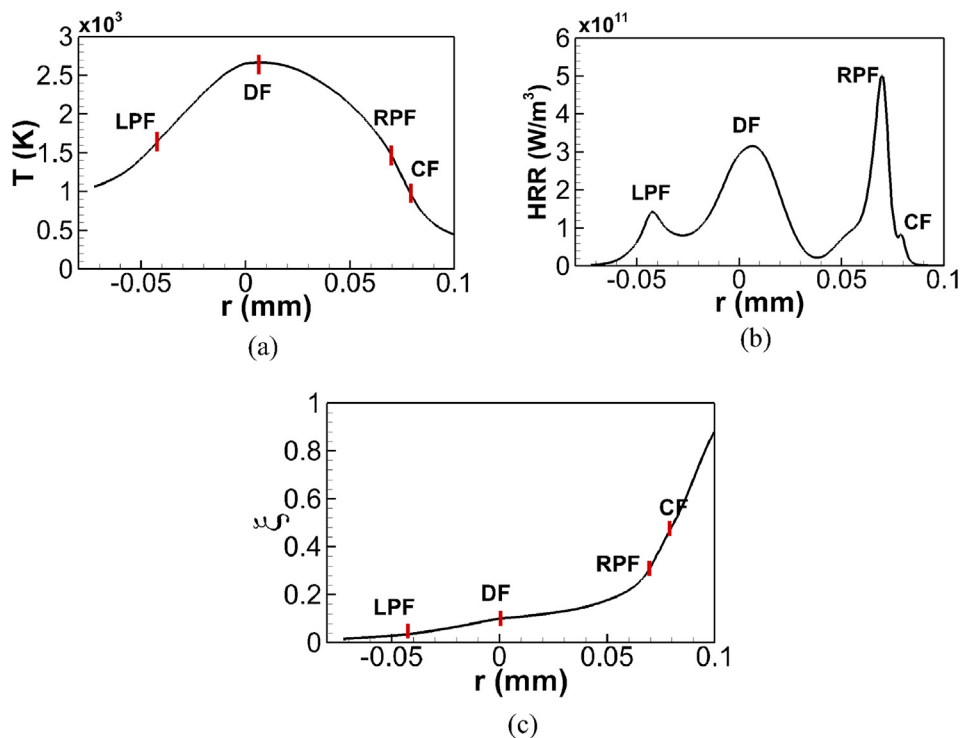


Fig. 4. Profiles of temperature (T), heat release rate (HRR) and mixture fraction (ξ) along the marked line A-A' in Fig. 3.

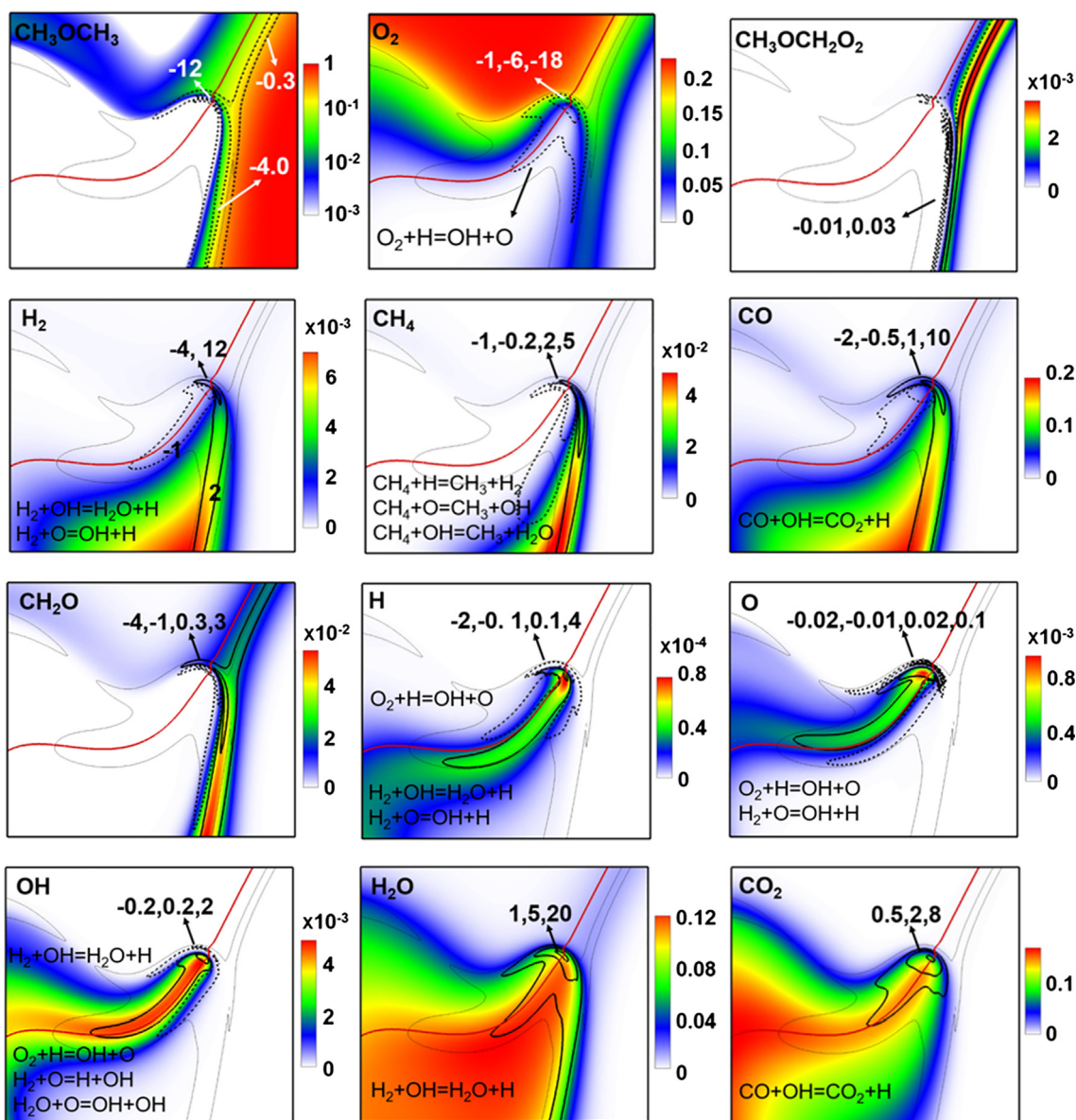


Fig. 5. Contours of mass fraction of reactants and products, superimposed with selected reaction rate isolines and the principal reaction steps at non-dimensional time $t^* = 1.54$. Black solid lines denote production rates, black dashed lines denote consumption rates ($\text{mol}/\text{cm}^3\text{s}$). Red solid line denotes the stoichiometric mixture fraction, while the thin gray solid line is the isoline of $\text{HRR} = 1 \times 10^{11} \text{ W}/\text{m}^3$, which qualitatively indicates the flame branches. (For interpretation of the references to colour in this figure legend, the reader is referred to the web version of this article.)

selected isolines of the corresponding reaction rates along with some principal reaction steps. The structures and reaction rates in the tetra-brachial flame exhibit significantly asymmetrical. Fig. 5 shows no leakage of the fuel (DME) beyond the primary premixed flame, however significant different magnitude of reaction rate of CH_3OCH_3 can be found at the branches of CF, RPF and LPF. In the cool flame branch upstream of the triple point, low temperature oxidation of DME is dominant, via the principal reactions as listed in Table 1 [14,35,36]. The low temperature chemistry is initiated by hydrogen abstraction (R1). The resulting CH_3OCH_2 species can then undergo oxygen addition via R2, R3, R4. At low temperatures R2 and R4 favour the forward direction, leading to chain branching and heat release. The temperature rise would result in the increase of reverse reaction rates of R2 and R4 due to temperature dependence of these reactions. On the other hand, the elevated temperature would favor the beta-scission process R5, which is the case inside the triple flame region. The thermal decomposition of species CH_3OCH_2 gradually increases via beta-scission, leading to build-up of radicals which attack the remaining fuel and

intermediate species. This eventually proceeds to a rapid thermal runaway associated with high temperature chemistry. The consumption rate of DME is significantly larger in the premixed flame branch than that in the cool flame branch, as shown in Fig. 5.

Inside the high temperature tribrachial flame, the remaining CH_3OCH_3 is decomposed into more stable fuels which include H_2 , CH_4 and CO , as shown in Fig. 5. CH_4 is further decomposed into H_2 and CO on the rich premixed flame side. The stable molecule H_2 and CO , which are produced on the fuel-rich side, are mainly oxidized by intermediate

Table 1
Low temperature oxidation of DME.

R1	$\text{CH}_3\text{OCH}_3 + \dot{\text{O}}\text{H} \rightarrow \text{CH}_3\text{OCH}_2 + \text{H}_2\text{O}$
R2	$\text{CH}_3\text{OCH}_2 + \text{O}_2 \leftrightarrow \text{CH}_3\text{OCH}_2\dot{\text{O}}_2$
R3	$\text{CH}_3\text{OCH}_2\dot{\text{O}}_2 \leftrightarrow \dot{\text{C}}\text{H}_2\text{OCH}_2\text{O}_2\text{H}$
R4	$\dot{\text{C}}\text{H}_2\text{OCH}_2\text{O}_2\text{H} + \text{O}_2 \leftrightarrow \dot{\text{O}}_2\text{C}\dot{\text{H}}_2\text{OCH}_2\text{O}_2\text{H}$
R5	$\dot{\text{C}}\text{H}_2\text{OCH}_2\text{O}_2\text{H} \rightarrow 2\dot{\text{C}}\text{H}_2\text{O} + \dot{\text{O}}\text{H}$

species OH and O in the diffusion flame. CO is consumed on the slightly fuel-lean side, primarily by OH in the water gas shift reaction, an important reaction contributing to the overall heat release rate. Radical species H, O and OH play an important role in the oxidization of fuels. H and O peak at the triple region, which incline to slightly rich and lean mixture respectively. This is because O_2 survives through the fuel-lean premixed flame and diffused toward the stable reactants from the fuel side and produces O through $O_2 + H = OH + O$. OH peaks along the mean reaction zone of the diffusion flame branch and contributes to the production of H_2O via $H_2 + OH = H_2O + H$ and CO_2 via $CO + OH = CO_2 + H$.

Modeling of tribrachial flames is still under development due to its complex structure of co-existing premixed and diffusion flames. It has been concluded that at least two variables are required to describe the chemical source terms, which depend on both mixing and reaction progress [37]. It is of great interest to parameterize the tetrabrachial flames based on the DNS results. As shown in Fig. 4, the mixture fraction varies monotonically across the tetrabrachial flames, which can be a measure of mixedness. Temperature can be a measure of the extent of reaction. Here, temperature and mixture fraction are adopted to parameterize the flame structure. The maximum consumption rates of O_2 in the premixed and the diffusion branches are superimposed to qualitatively demonstrate the locations of the three branches of the flame. O_2 is adopted here because it is the only reactant which is consumed in both the premixed and diffusion flames, as used in [34]. Fig. 6 shows isocontours of mass fraction of reactants and products, overlaid with selected reaction rate isolines in ξ - T phase space. Data is extracted from the same physical region shown in Fig. 5. The figures help to highlight the different topologies of the flame which may be not apparent in physical coordinates. The asymmetrical structures of the flame, like shifts in reactant concentration or reaction peaks on the lean and rich sides and the declination between diffusion and premixed branches, are more distinct in the ξ - T phase space. CH_3OCH_3 is

consumed in the premixed flame branches with negligible leakage to the trailing diffusion flame. $CH_3OCH_2O_2$ is produced and consumed under low temperature. OH is produced and enriched around the diffusion flame. H_2 is produced in the premixed flame and consumed in diffusion branch. H_2 is concentrated around the fuel-rich premixed branch. The peak consumption of O_2 and production of H_2O occur at the triple point H_2O is enriched in fuel-rich mixtures.

3.3. Turbulence effects on auto-ignition

Turbulence, which generates a range of χ values, has been observed to affect the location and timing of autoignition in the mixing layer. In this section, we analyze the influence of varied turbulence length scales on the two-stage ignition, while keeping other parameters unchanged. The initial turbulence integral length scale l_t increases from 0.1 (case 1) to 0.2, and 0.4 mm for cases 2&3, respectively. A similar two-stage ignition process can be found in cases 2&3 with different turbulence length scales, as shown in Fig. 7. The first stage ignition front presents to be connected, compared with the disconnected front found in case 1. The larger turbulence scales in cases 2&3 reduce the scalar gradient, resulting in a decreased scalar dissipation rate. The first high-temperature ignition kernels (HIKs) also form in the rich mixture regions close to the black solid lines (isoline of $\xi_{mr,1d}$). Less kernels are observed for cases 2&3 with larger turbulent scales.

It has been qualitatively shown that high temperature kernels are spatially distributed around the $\xi_{mr,1d}$ surface. Fig. 8a shows the instantaneous scalar dissipation rate field just before the occurrence of the first ignition kernel, superimposed with all ignition kernels found during the ignition process in case 1. As in [27], an ignition kernel is defined as a local maximum of HRR which emerges from a point-source due to autoignition. The kernel formation is defined as the instant at which the peak in HRR exceeds $4 \times 10^{11} \text{ W/m}^3$. Note that the scalar dissipation rate would vary with time and the ones shown in Fig. 8a are

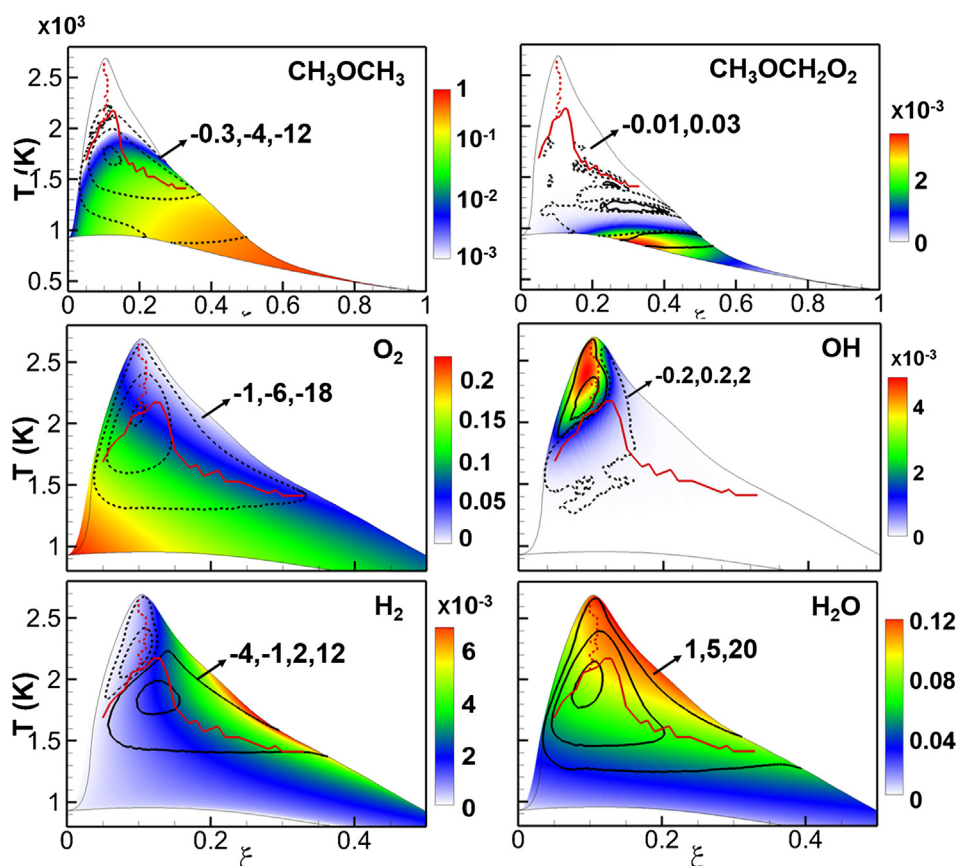


Fig. 6. Contours of mass fraction of reactants and products, superimposed with selected reaction rate isolines in ξ - T phase space. Data is extracted from the same physical region in Fig. 4. Black solid lines denote production rates, black dashed lines denote consumption rates ($\text{mol}/\text{cm}^3\text{s}$). Red solid line qualitatively denotes the premixed flame branches, red dashed line denotes the diffusion flame branch. (For interpretation of the references to colour in this figure legend, the reader is referred to the web version of this article.)

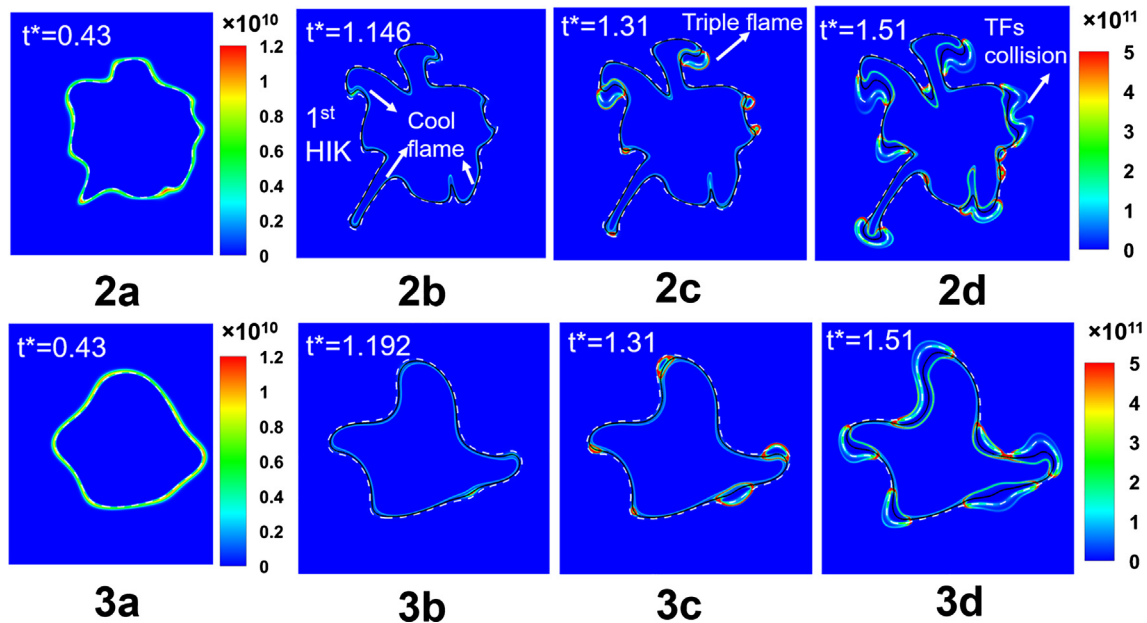


Fig. 7. Temporal evolution of heat release rate for case 2&3 with different turbulence length scales (HRR), W/m^3 . The non-dimensional time $t^* = t/\tau_{(\xi=\xi_{mr,0d})}$. The white dashed line is the ξ_{st} surface and the black solid line is the $\xi_{mr,1d}$ surface, which is related to the second stage ignition of the 1d mixing layer.

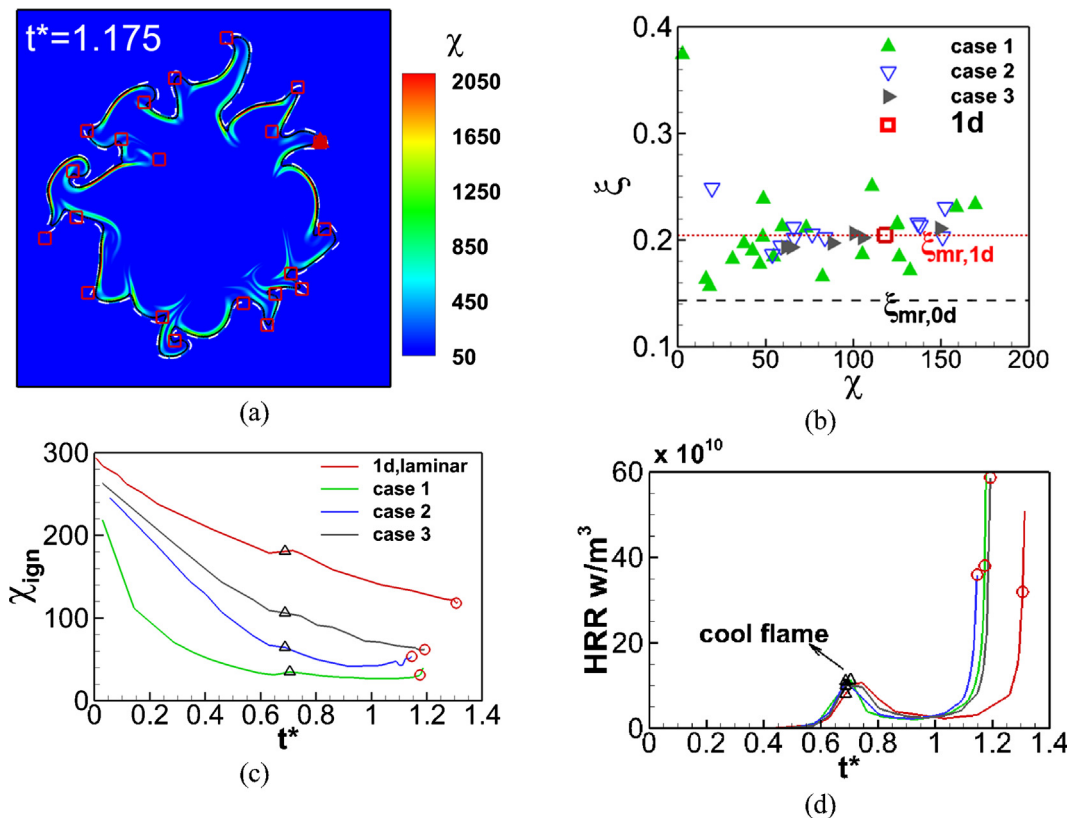


Fig. 8. (a) Instantaneous scalar dissipation rate field when the first high temperature ignition kernel occurs; (b) mixture fraction and the corresponding scalar dissipation rate at high temperature kernels; (c) history of local scalar dissipation rate; and (d) local heat release rate at the first high temperature ignition kernels.

not the corresponding χ to the final ignition of the kernels. Turbulence creates a wide range of χ , including well mixed spots with low $\chi|\xi_{mr}$, as well as high strained regions with high $\chi|\xi_{mr}$ and large heat loss. The high temperature ignition (also the first stage low temperature auto-ignition) is favored by low χ with low heat losses. The detailed mixture fraction ξ_{ign} and the corresponding χ_{ign} at the ignition kernels are shown in Fig. 8b. Kernels are found to form over a wide range of the

mixture fraction. Especially for case a with the smallest initial turbulent length scale, most ξ_{ign} varies between 0.156 and 0.250, except one occurring at very rich mixture with $\xi_{ign} = 0.374$, which is caused by the collision of cool flames. Compared with $\xi_{mr,0d}$, $\xi_{mr,1d}$ is much closer to ignition mixture fraction ξ_{ign} , especially for case c with the largest turbulence scale. The largest variance of ξ_{ign} compared with $\xi_{mr,1d}$ is around 25%, excluding the specific ignition kernel in very rich mixture

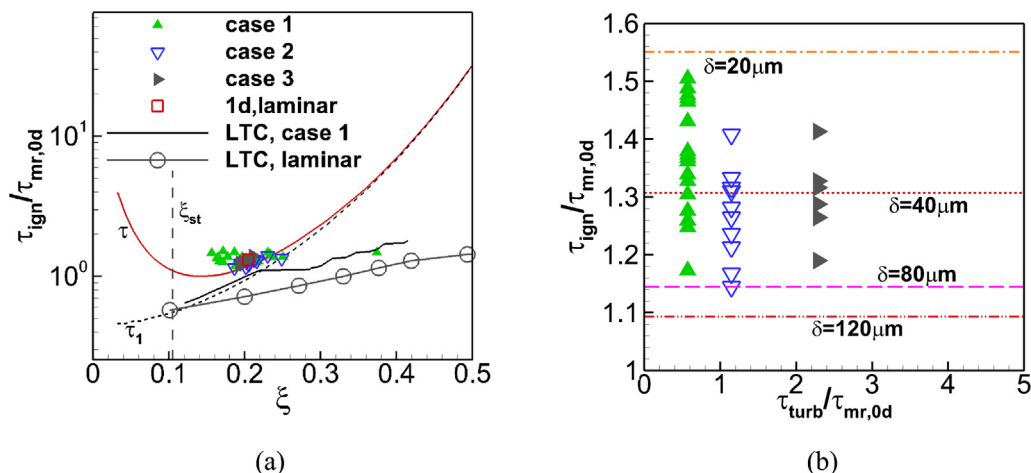


Fig. 9. (a) Comparison of τ_1 and τ with the mean cool-flame and ignition kernels; (b) ignition time of high temperature kernels τ_{ign} against τ_{turb} , normalized by $\tau_{mr,0d}$, including results of 1d laminar mixing layers with varied initial mixing layer thickness δ .

caused by cool flames interaction. Time records of the local scalar dissipation rate χ and heat release rate at the first ignition kernels are compared in Fig. 8c & d. Mixing and reaction help to smooth the scalar gradient and reduce the local scalar dissipation rate, which is enhanced in turbulent flows and results in a faster decrease of χ . Thus, ignition tends to be faster than that in the laminar case from the same initial state as in Fig. 8d.

In Fig. 9a, the time instants at which high temperature autoignition kernels occur, are compared with the first stage (τ_1) and second stage (τ) ignition delay time measured in the homogeneous reactor. The second ignition delay times for the cases studied are larger than $\tau_{(\xi=\xi_{mr,0d})}$. However, they are found to be comparable with the corresponding laminar delay time $\tau_{(\xi=\xi_{mr,1d})}$. The mean location of the cool flame and its propagation in ξ -space are also compared in Fig. 9a. It is observed that the cool flame proceeds rapidly into the rich mixtures.

The high temperature autoignition delay times would be affected by turbulence. Fig. 9b shows calculated autoignition times from the three turbulent simulation cases, as well as several simulations of 1d laminar mixing layers with different initial thicknesses δ . It can be found that increasing δ results in earlier ignition. For turbulent cases, $\tau_{ign}/\tau_{mr,0d}$ varies between 1.14 and 1.5. Turbulent flows ignite earlier than laminar ones with the same δ . Turbulent mixing induces the minimum value of $\chi|_{\xi_{mr}}$ which is smaller than that in the corresponding laminar flow. The number of ignition kernels depends on the turbulence scales, however, the occurrence of the first ignition kernel does not significantly change with variation of τ_{turb} .

4. Conclusions

Direct numerical simulations have been performed to clarify the influence of turbulence on the timing and location of two-stage ignition of the DME/air mixture under diesel engine relevant conditions. Three cases with different initial turbulent integral length scales are investigated. A typical sequence of events is firstly visualized to describe the temporal and spatial evolution of the two-stage ignition. Qualitatively, the first stage of autoignition is initiated in the lean mixtures, and thereafter the flame kernel develops into a diffusion-supported cool flame which propagates into the rich mixtures. The second stage of autoignition is spatially distributed in the fuel-rich mixtures. The ignition kernels rapidly expand and establish tetrabrachial edge flames, propagating in opposite directions along the ξ_{st} surface. The transition from autoignition kernels to edge flame propagation is similar for the three cases but more kernels are observed for the cases with smaller scales of turbulence.

The detailed chemical structures of tetrabrachial flames are

analyzed in terms of reactant concentrations and the reaction rate profiles. The cool flame branch is dominated by low temperature reactions, while the other three branches are mainly involved in high temperature oxidation of the remaining fuel and intermediate species. The excess DME is consumed in the premixed flame branches with negligible leakage to the trailing diffusion flame, where it is decomposed into more stable fuels including H_2 , CH_4 and CO . In the diffusion flame, H_2 and CO are mainly oxidized by intermediate species OH and O . The structures and reaction rates in the tetrabrachial flame exhibit significant asymmetry, which is more distinct in the mixture fraction-temperature phase space.

High temperature kernels occur in a variety of ignition times and locations. Examination of the statistics of high temperature kernels shows that a most reactive mixture fraction $\xi_{mr,1d}$ determined from laminar autoigniting mixing layers is more appropriate to predict the locations of autoignition than that calculated from the homogeneous reactor model. The spatial scatter of ignition sites is due to the random spatial distribution of regions with $\xi = \xi_{mr,1d}$ and low χ . The high temperature ignition in turbulent flows is observed to be more advanced than the corresponding laminar case but the second ignition delay times for the different turbulent cases studied do not deviate a lot. The exact locations of kernel formation are important for the overall ignition and stabilization processes.

Acknowledgements

This work is supported by the National Natural Science Foundation of China (No. 51576176). Supercomputing time on ARCHER provided under the UK Engineering and Physical Sciences Research Council (EPSRC) projects “UK Consortium on Mesoscale Engineering Sciences (UKCOMES)” (Grants No. EP/L00030X/1 and No. EP/R029598/1) and “High Performance Computing Support for United Kingdom Consortium on Turbulent Reacting Flow (UKCTRF)” (Grant No. EP/K024876/1) is gratefully acknowledged.

Appendix A. Supplementary data

Supplementary data associated with this article can be found, in the online version, at <http://dx.doi.org/10.1016/j.fuel.2018.05.118>.

References

- [1] Pickett LM, Kook S, Williams TC. SAE Int J Engines 2009;2:439–59.
- [2] Musculus MPB, Miles PC, Pickett LM. Prog Energy Combust Sci 2013;39:246–83.
- [3] Maes N, Meijer M, Dam N, Somers B, Baya Toda H, Bruneaux G, et al. Combust Flame 2016;174:138–51.

- [4] Donkerbroek AJ, van Vliet AP, Somers LMT, Dam NJ, ter Meulen JJ. *Combust Flame* 2011;158:564–72.
- [5] Singh S, Musculus MPB, Reitz RD. *Combust Flame* 2009;156:1898–908.
- [6] Vervisch L, Poinot T. *Annu Rev Fluid Mech* 1998;30:655–91.
- [7] Domingo P, Vervisch L. *Symp (Int) Combust* 1996;26:233–40.
- [8] Echehki T, Chen JH. *Proc Combust Inst* 2002;29:2061–8.
- [9] Buckmaster J. *Prog Energy Combust Sci* 2002;28:435–75.
- [10] Chung SH. *Proc Combust Inst* 2007;31:877–92.
- [11] Choi BC, Chung SH. *Combust Flame* 2012;159:1481–8.
- [12] Choi BC, Kim KN, Chung SH. *Combust Flame* 2009;156:396–404.
- [13] Law CK, Zhao P. *Combust Flame* 2012;159:1044–54.
- [14] Krisman A, Hawkes ER, Talei M, Bhagatwala A, Chen JH. *Proc Combust Inst* 2015;35:999–1006.
- [15] Deng S, Zhao P, Mueller ME, Law CK. *Combust Flame* 2015;162:3437–45.
- [16] Deng S, Zhao P, Mueller ME, Law CK. *Combust Flame* 2015;162:4471–8.
- [17] Krisman A, Hawkes ER, Talei M, Bhagatwala A, Chen JH. *Combust Flame* 2016;172:326–41.
- [18] Mastorakos E, Baritaud TA, Poinot TJ. *Combust Flame* 1997;109:198–223.
- [19] Mukhopadhyay S, Abraham J. *Proceedings of the institution of mechanical engineers. D J Automob Eng* 2012;227:748–60.
- [20] Hilbert R, Thevenin D. *Combust Flame* 2002;128:22–37.
- [21] Im HG, Chen JH, Law CK. *Twenty-Seventh Symposium (International) on Combustion*, vols. 1 and 2. 1998. p. 1047–56.
- [22] Sreedhara S, Lakshmisha KN. *Proc Combust Inst* 2000;28:25–33.
- [23] Kerkemeier SG, Markides CN, Frouzakis CE, Boulouchos K. *J Fluid Mech* 2013;720:424–56.
- [24] Mastorakos E. *Prog Energy Combust Sci* 2009;35:57–97.
- [25] Yao T, Yang WH, Luo KH. *Comput Fluids* 2018. <http://dx.doi.org/10.1016/j.compfluid.2018.03.075>.
- [26] Borghesi G, Mastorakos E, Cant RS. *Combust. Flame* 2013;160:1254–75.
- [27] Krisman A, Hawkes ER, Talei M, Bhagatwala A, Chen JH. *Proc Combust Inst* 2017;36:3567–75.
- [28] Krisman A, Hawkes ER, Chen JH. *J Fluid Mech* 2017;824:5–41.
- [29] Robert FMR, Kee J, Meeks Ellen, Miller James A. *CHEMKIN-III: A fortran chemical kinetics package for the analysis of gas phase chemical and plasma kinetics*. Sandia National Laboratories Report 1996.
- [30] Jin T, Luo K, Lu S, Fan J. *Int J Hydrogen Energy* 2013;38:9886–96.
- [31] Luo K, Wang H, Yi F, Fan J. *Energy Fuels* 2012;26:6118–27.
- [32] Bansal G, Mascarenhas A, Chen JH. *Combust Flame* 2015;162:688–702.
- [33] Choi SK, Kim J, Chung SH, Kim JS. *Combust Theor Model* 2009;13:39–56.
- [34] Echehki T, Chen JH. *Combust Flame* 1998;114:231–45.
- [35] Curran HJ, Fischer SL, Dryer FL. *Int J Chem Kinet* 2000;32:741–59.
- [36] Zheng XL, Lu TF, Law CK, Westbrook CK, Curran HJ. *Proc Combust Inst* 2005;30:1101–9.
- [37] Owston R, Abraham J. *Int J Hydrogen Energy* 2011;36:8570–82.